Check for updates

small methods
www.small-methods.com

Synthesis of Microscopic 3D Graphene for High-Performance Supercapacitors with Ultra-High Areal Capacitance

Viet Hung Pham, Congjun Wang, Yuan Gao, Jennifer Weidman, Ki-Joong Kim, and Christopher Matranga*

Despite graphene being considered an ideal supercapacitor electrode material, its use in commercial devices is limited because few methods exist to produce high-quality graphene at a large scale and low cost. A simple method is reported to synthesize 3D graphene by graphenization of coal tar pitch with a K_2CO_3 catalyst. This produces 3D graphenes with high specific surface areas up to 2113 m^2 g^{-1} and exceptional crystallinity (Raman I_D/I_G as low as ≈0.15). The material has an outstanding specific capacitance of 182.6 F g^{-1} at a current density of 1.0 A g^{-1}. This occurs at a mass loading of 30 mg cm^{-2} which is 3 times higher than commercial requirements, yielding an ultra-high areal capacitance of 5.48 F cm^{-2}. The K_2CO_3 is recycled and reused over 10 cycles with material quality and electrocapacitive performance of 3D graphene retained and verified after each cycle. The synthesis method and resulting electrocapacitive performance properties create new opportunities for using 3D graphene more broadly in practical supercapacitor devices.

1. Introduction

The growth of renewable energy has accelerated in recent years, in part, due to the decreasing cost of renewable energy sources and the global drive to decarbonize the energy economy. A key technology for addressing the intermittent and distributed nature of renewables is the development of efficient and reliable energy storage systems that can reduce curtailment, match electricity demand with grid capacity, and improve grid performance and reliability.[1–4]

Supercapacitors, also called electrochemical capacitors, have attracted attention for grid-scale applications due to their high power density, reasonable energy densities, fast charge/discharge rates, low cost, and ultralong cycle life.[2,3] These devices bridge a gap between conventional capacitors and traditional batteries by storing more energy than capacitors and possessing higher power densities than batteries. Ideal supercapacitor electrode materials must have a high specific surface area, a pore size distribution that allows electrolyte ions to diffuse into accessible pores and form an electrochemical double layer (EDL), and good electrical conductivity for electron transfer.[5–9]

Graphene is one of the most promising supercapacitor electrode materials because of its large surface area, high electrical conductivity, good chemical stability, and excellent mechanical strength. Its theoretical specific capacitance is ≈550 F g^{-1} which is higher than all other carbon-based materials.[6–10] One challenge with using graphene in practical supercapacitors is that fully exfoliated graphene sheets restack and form aggregated graphite-like powders or films due to strong sheet-to-sheet van der Waals interactions, which decreases surface area and reduces ion diffusion rates, resulting in unsatisfactory capacitances and poor rate performance. One way to address this challenge is to construct the 2D graphene sheets into a well-organized and interconnected, porous, 3D structure that prevents sheet restacking and preserves the electrical properties while enabling a large accessible internal surface area, efficient mass transport, and high electron conduction.[10,11]

Several fabrication techniques have been reported for 3D graphene (3DG) including self-assembly and reduction of graphene oxide (GO),[12,13] chemical vapor deposition of gaseous hydrocarbons on 3D structured substrates,[14] on-site polymerization (OSP) of nongaseous hydrocarbons and chemical reduction of inorganic carbon compounds (CO_2, CO or CS_2) with alkali, alkali oxide and alkaline earth metals.[15–17] All these methods are promising, but their use for practical supercapacitors is limited by the complexity of the procedure, cost and/or availability of feedstocks, mass yield

V. H. Pham, C. Wang, Y. Gao, J. Weidman, K.-J. Kim, C. Matranga
National Energy Technology Laboratory
626 Cochran Mill Road, Pittsburgh, PA 15236, USA
E-mail: viethung.pham@netl.doe.gov
V. H. Pham, Y. Gao, J. Weidman, K.-J. Kim
NETL Support Contractor
626 Cochran Mill Road, Pittsburgh, PA 15236, USA
The ORCID identification number(s) for the author(s) of this article can be found under https://doi.org/10.1002/smtd.202301426

© 2024 The Authors. Small Methods published by Wiley-VCH GmbH. This is an open access article under the terms of the Creative Commons Attribution-NonCommercial-NoDerivs License, which permits use and distribution in any medium, provided the original work is properly cited, the use is non-commercial and no modifications or adaptations are made.

DOI: 10.1002/smtd.202301426

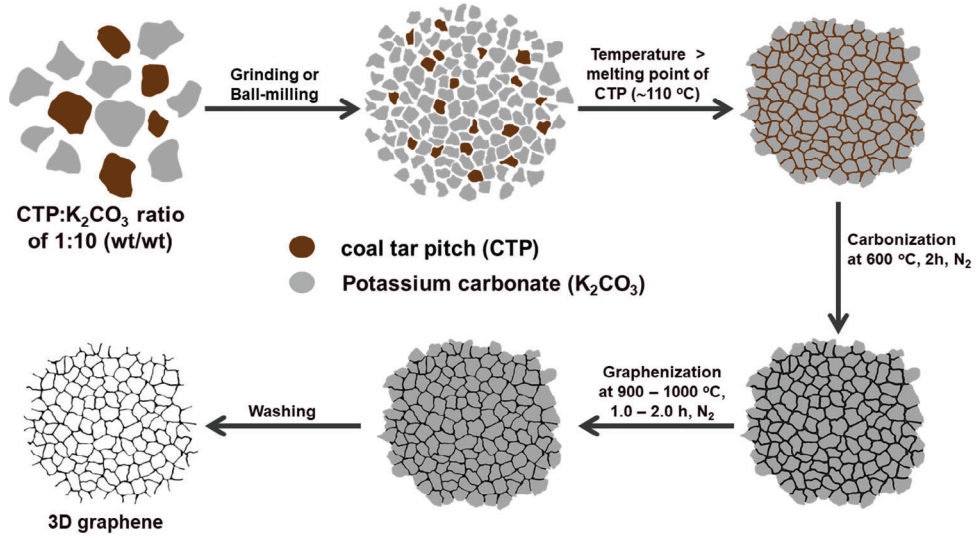

Figure 1. Schematic illustration of the synthesis process of 3D graphene.

of carbon product, and/or the quality of the 3D graphene produced.[10]

We report a method that uses an inexpensive and abundant carbon feedstock, coal tar pitch (CTP), along with a potassium carbonate (K_2CO_3) catalyst in a simple, tube-furnace based, process to make microscopic 3D graphenes with carbon mass yields as high as ≈37%. The quality of these 3D graphenes is indicated by Raman I_D/I_G ratios as low as 0.15 and the highest specific surface area reported for this material, yet, at 2113 $m^2\ g^{-1}$. The K_2CO_3 catalyst was recycled at a mass recovery rate of 95% which was demonstrated for 10 full cycles with the quality of 3D graphene retained after each cycle. This material has outstanding electrochemical capacitive properties with a gravimetric specific capacitance of 182.6 F g^{-1} at a current density of 1.0 A g^{-1}. This is unique because it is achieved at a mass loading of 30 mg cm^{-2}, which is 3 times higher than current commercial requirements for practical supercapacitor devices, resulting in ultra-high areal capacitance of 5.48 F cm^{-2}. These capacitive properties are among the highest, if not the highest, ever reported for graphene-based supercapacitor devices.

Our results overcome a long-standing challenge for fabricating practical supercapacitor electrodes which involves balancing two conflicting characteristics: high porosity and high material density.[9] We directly address this challenge by producing an electrically conductive 3D graphene possessing a pore structure that does not collapse under harsh compression giving it both high porosity and reasonable packing density.[10,18,19] This allows for the high electron and ion transport rates needed to achieve outstanding electrocapacitive properties at ultrahigh mass loadings. Achieving these properties at ultrahigh mass loading overcomes the dilution of gravimetric energy and power densities that occurs in practical supercapacitor devices from the additional weight of current collectors, separators, electrolytes, binders, connectors, and packaging.[7–9,20] As such, our simple synthesis method allows for the inexpensive production of electrodes and opens new opportunities for using graphene-based materials more broadly in practical supercapacitor devices.

2. Results and Discussion

2.1. Synthesis and Characterization of 3D Graphene

The synthesis process of microscopic 3D graphene by catalytic graphenization is schematically illustrated in **Figure 1**. CTP is first homogeneously dispersed in K_2CO_3 by ball milling for 15 min with a mass ratio of CTP:K_2CO_3 at 1:10. This solid mixture is then heated beyond the melting point of CTP (≈110 °C) which converts the CTP into a liquid that coats K_2CO_3 particles and infiltrates the spaces between them. The mixture is then heated to 600 °C under a nitrogen atmosphere, which carbonizes the melted CTP and causes the formation of an interconnected 3D network of carbon nanosheets as evidenced by SEM and Raman characterization (Figure S1, Supporting Information). The sample is then heated to 900–1000 °C, which leads to the catalytic conversion of carbon nanosheets into graphene nanosheets.[21] Afterward, the K_2CO_3 is rinsed away with water and recovered for recycling and reuse (details below) and the product is dried, which leaves behind fluffy carbon powders with tap densities as low as 0.035 g cm^{-3}, indicating a highly porous structure (Figure S2, Supporting Information). The synthesis yield, on a carbon basis, at 900, 950, and 1000 °C (denoted as 3DG-900, 3DG-950, and 3DG-1000) were 36.8, 33.2, and 32.7 wt%, respectively. Using longer graphenization times causes a dramatic reduction in the carbon yield and surface area of the sample. Additionally, using CTP:K_2CO_3 mass ratios that are below 1:10 still results in microscopic 3D graphitic porous carbons whereas using a higher mass ratio leads to lower production yield (Figure S3, Supporting Information).

Scanning electron microscopy (SEM) images of the 3DG samples (**Figure** 2a–c) show hierarchical, interconnected, 3D networks of thin, crumpled, graphene sheets. This network possesses irregularly shaped, macro- and meso-scale pore structures with sizes ranging from a few microns down to tens of nanometers. The shape and size of these macro- and meso-scale structures result, in part, from the shape of K_2CO_3 particles and their templating role during the carbonization step which is confirmed

 © 2024 The Authors. Small Methods published by Wiley-VCH GmbH

23663608, 0, Downloaded from https://onlinelibrary.wiley.com/doi/10.1002/smtd.202301426 by National Energy Technology Laboratory, Wiley Online Library on [11/06/2024]. See the Terms and Conditions (https://onlinelibrary.wiley.com/terms-and-conditions) on Wiley Online Library for rules of use; OA articles are governed by the applicable Creative Commons License

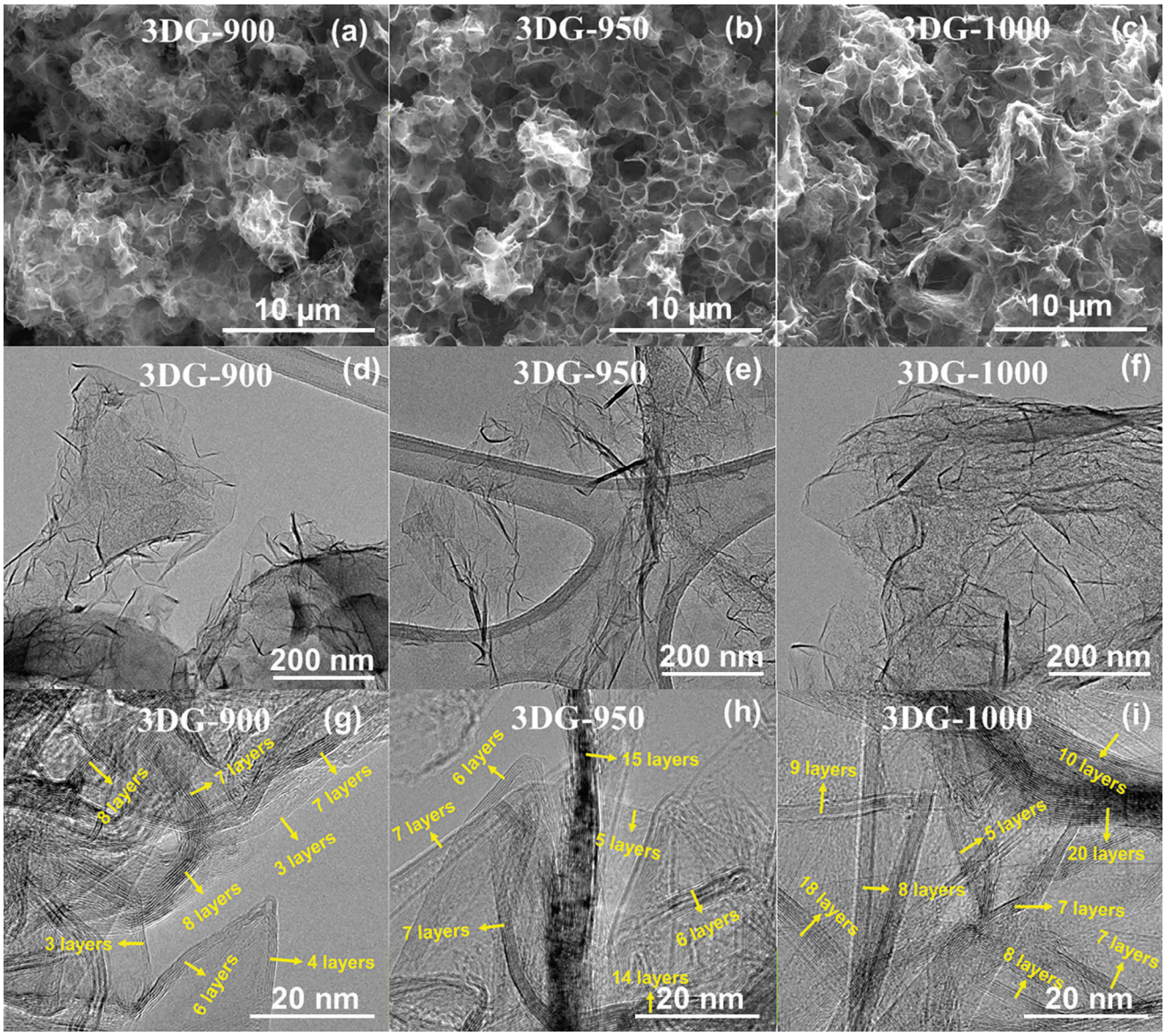

Figure 2. a–c) SEM and d–i) TEM images of 3DGs.

by experiments with varying particle sizes (Figure S4, Supporting Information) to create larger macro- and meso- scale structures in the final carbon product. The transmission electron microscopy (TEM) images in Figure 2d–f illustrate the microstructure is composed of stacks of graphene sheets with fewer layers at lower synthesis temperatures and more layers at higher synthesis temperatures. The number of graphene layers is estimated from high-resolution TEM (HR-TEM) lattice fringes in Figure 2g–i: 1) 3–8 layers for 3GD-900, 2) 5–15 layers for 3GD-950, and 3) 5–20 layers for 3DG-1000. The variation of graphene layers with synthesis temperature can be explained by the molten K_2CO_3 viscosity. At 900 °C, which is slightly above the K_2CO_3 melting point (891 °C), the molten salt has a higher viscosity, limiting the movement of graphene sheets that are formed, as well as their restacking to generate thicker microstructures. However, at higher temperatures, the lower viscosity of the molten salt allows graphene sheets that are formed to move more freely, leading to additional restacking which increases the number of graphene sheets observed in the microstructure of these 3DGs.[22]

The datasets shown in **Figure 3** illustrate that the 3DG samples are exceptionally high quality. The Raman spectra (Figure 3a) show that the I_D/I_G ratio (**Table 1**) varies from 0.59 for 3DG-900 to only 0.15 for 3DG-1000, which is significantly lower than comparable graphene materials (Table S1, Supporting Information)[13–15,21,23–29] and approaches that of a commercially available graphite sample with an I_D/I_G of 0.17 (Figure S5, Supporting Information). The XPS survey spectra (Figure 3b) show the prominent C1s peaks and minor O1s peaks, yielding an oxygen atomic percentage of only 1.6–2.1%. This produces a C/O ratio that varies from 44.6 to 61.5 for these samples and is far higher than comparable graphene materials (Table S1, Supporting Information). The deconvoluted C1s spectra (Figure 2c; Figure S6,

 © 2024 The Authors. Small Methods published by Wiley-VCH GmbH

23663608, 0, Downloaded from https://onlinelibrary.wiley.com/doi/10.1002/smtd.202301426 by National Energy Technology Laboratory, Wiley Online Library on [11/06/2024]. See the Terms and Conditions (https://onlinelibrary.wiley.com/terms-and-conditions) on Wiley Online Library for rules of use; OA articles are governed by the applicable Creative Commons License

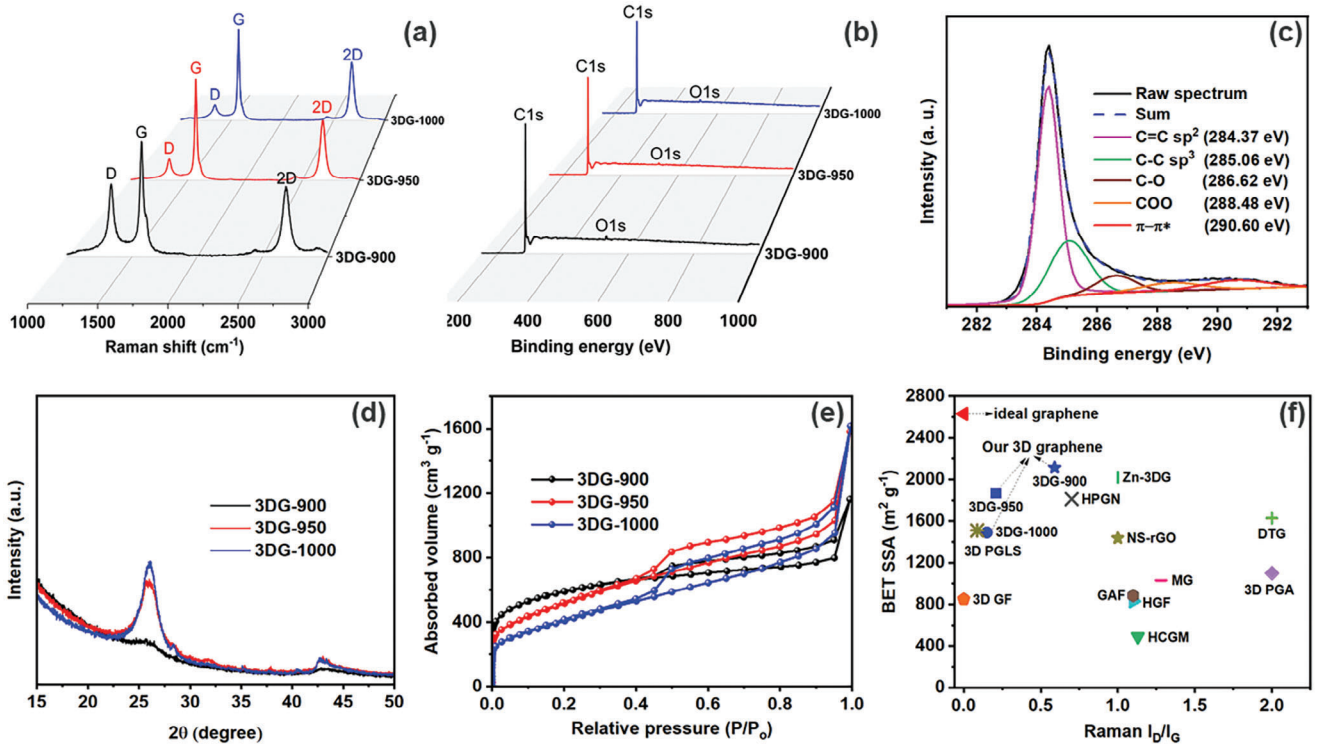

Figure 3. a) Raman spectra, b) survey XPS spectra, c) deconvoluted C1s XPS spectrum of 3DG-950, d) XRD patterns, e) N_2 adsorption-desorption isotherms of 3D graphenes and f) comparison of BET SSA and Raman I_D/I_G of 3D graphene with other graphenes with high SSA. (Holey graphene framework (HGF),[13] 3D porous graphene-like sheets (3D PGLS),[21] Highly compressible graphene monolith (HCGM),[23] 3D printed graphene aerogels (3D PGA),[24] Wet-spun graphene core-shell aerogel fiber (GAF),[25] Non-stacked rGO (NS-rGO),[26] 3D graphene foam (3D GF),[14] Unstacked double layer templated graphene (DTG),[27] Hierarchical porous graphene networks (HPGN),[28] Microporous graphene (MG),[15] Zn-guided 3D graphene (Zn-3DG)).[29]

Supporting Information) demonstrate that the C_{sp2} contribution to the total C1s lineshape is: 1) 57.2% for 3DG-900, 2) 70.3% for 3DG-950, and 3) 73.1% for 3DG-1000. XRD patterns exhibit broad (002) peaks at ~26°, which result from the thin crystalline graphene sheets in the sample. The intensity of the (002) peak increases with the graphenization temperature, due to the thickness of the graphene sheet structures, which is also consistent with the micrographs shown in Figure 2g–i.

N_2 isotherms (Figure 3e) display combined type I(b) and type IV(a) characteristics, indicating a hierarchical pore structure consisting of macro-, meso-, and micro-pores.[30–32] The total pore volumes estimated at a relative pressure of 0.995 were 1.80, 2.45, and 2.50 $cm^3\ g^{-1}$ for 3DG-900, 3DG-950, and 3DG-1000, respectively. Specific surface areas (SSA) calculated by the Brunauer–Emmett–Teller (BET) method were 2113, 1866, and 1490 $m^2\ g^{-1}$ for 3DG-900, 3DG-950, and 3DG-1000, respectively, and are higher than previous literature reports for comparable materials (Figure 3f and Table 1; Table S1, Supporting Information). Notably, 3DG-900 has the highest BET SSA reported for 3D graphene materials (Table S1, Supporting Information). The outstanding specific surface area of 3DG-900 is mainly caused by a high fraction of micropores in the pore structure (Figure S7, Supporting Information). At higher graphenization temperatures, the reconstruction of the microstructure of graphene sheets due to the lower viscosity of molten salt resulted in a lower micropore volume with a significant increase of mesopore and macropore volumes, leading to a decrease of BET SSA.

Table 1. Production yield and properties of 3DGs.

	BET SSA [$m^2\ g^{-1}$]	QSDFT micropore volume [$cm^3\ g^{-1}$]	QSDFT mesopore volume [$cm^3\ g^{-1}$]	BJH macropore volume [$cm^3\ g^{-1}$][a)]	Total pore volume [$cm^3\ g^{-1}$][b)]	Average Raman I_D/I_G[c)]	XPS atomic C/O ratio	Production yield [wt%]
3DG-900	2113	0.59	0.78	0.39	1.80	0.59	46.6	36.8
3DG-950	1866	0.35	1.47	0.65	2.45	0.21	51.6	33.2
3DG-1000	1490	0.23	1.54	0.82	2.50	0.15	61.5	32.7

[a)] Volume of macropore with size of 50–200 nm was calculated from the adsorption data by BJH method; [b)] Total pore volume at P/Po = 0.995; [c)] Average Raman I_D/I_G was calculated from spectra measured at 5 different positions.

© 2024 The Authors. Small Methods published by Wiley-VCH GmbH

23663608, 0, Downloaded from https://onlinelibrary.wiley.com/doi/10.1002/smtd.202301426 by National Energy Technology Laboratory, Wiley Online Library on [11/06/2024]. See the Terms and Conditions (https://onlinelibrary.wiley.com/terms-and-conditions) on Wiley Online Library for rules of use; OA articles are governed by the applicable Creative Commons License

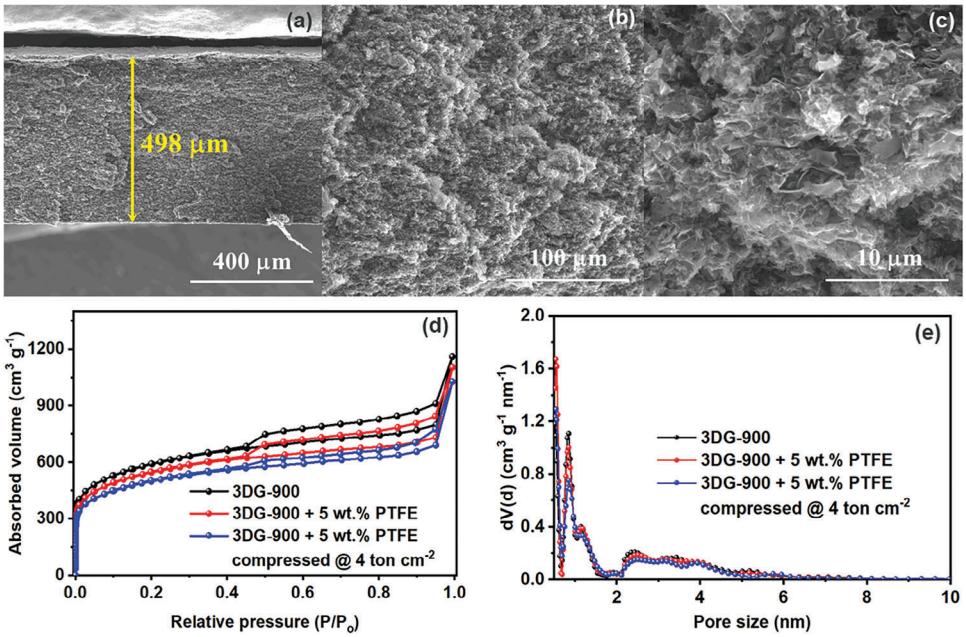

Figure 4. a) Cross-section SEM image of 3DG-900 electrode with mass loading of 20 mg cm^{-2}, b,c) SEM zoom-in images of (a), d) N_2 isotherms of 3DG-900, 3DG-900 and 5.0 wt% PTFE binder and 3DG-900 electrode with mass loading of 20 mg cm^{-2}.

Figure 3f directly compares the BET SSA and Raman I_D/I_G of the 3DG sample from this report to existing literature and illustrates the properties of our 3DG exceed previous reports and start to approach those of ideal graphene. As expected for a highly crystalline carbon, the electrical conductivity of the samples with 5 wt% polytetrafluoroethylene (PTFE) binder compressed at 4.0 ton cm^{-2} was 1295, 1933 and 2370 S cm^{-1} for 3DG-900, 3DG-950, and 3DG-1000, respectively.

2.2. Electrochemical Capacitive Performance of 3DG Supercapacitors

The microstructure, crystallinity, porosity, and electrical conductivity of the 3DGs make them exceptional candidates for supercapacitor applications. 3DG-900 electrodes were fabricated using 95 wt% of 3DG-900 as active electrode material and 5.0 wt% PTFE as a binder without using any conductive additive. 3DG-900 and PTFE were compressed at 4.0 ton cm^{-2} into compact pellet electrodes with mass loading of 5.0, 10, 20 and 30 mg cm^{-2}. Most literature reports use mass loadings of 1.0–5.0 mg cm^{-2}, whereas the current requirement for fabricating commercial devices is ≥10.0 mg cm^{-2}.[7–9] As such, our results at mass loadings of 10–30 mg cm^{-2} are directly relevant to fabricating and engineering practical supercapacitor devices.

Compression of the 3DG-900 at 4 tons cm^{-2} with PTFE binder did not adversely affect the structure or porosity of the active electrode material. SEM images (**Figure 4**a–c; Figure S8, Supporting Information) show that 150–770 micron-thick electrodes retain the hierarchical, interconnected, network of graphene sheets, as well as the macro- and meso-porosity noted in Figure 3a for the as-synthesized material. The N_2 isotherms and pore size distributions (Figure 4d,e) were essentially unchanged as evidenced by total pore volumes and BET SSA which only decreased by ≈9% and ≈15%, respectively (Table S2, Supporting Information). The minor decrease in SSA, total pore volume as well as pore size distribution despite the harsh electrode fabrication process indicates the micro-structure of 3DG-900 is largely preserved. The existence of a highly hierarchical micro-, meso-, and macro-porous structure is highly desired, especially for a thick electrode, since it facilitates electrolyte ion diffusion throughout the electrode, which enhances electrochemical performance.

The performance of the 3DG-900 as a supercapacitor electrode was evaluated in two-electrode symmetric cells using 6 M KOH aqueous electrolyte. Taking advantage of the chemically inert surface of 3DG-900 with very low oxygen content, 3DG-900 supercapacitors were tested at an extended working voltage of 0–1.2 V (instead of 0–1.0 V) which could increase the energy density by up to 44%.[38–41] For comparison, we also conducted tests that restricted the working voltage of 0–1.0 V which yielded nearly identical electrochemical performance except with a lower energy density (Figure S9, Supporting Information).

Cyclic voltammetry (CV) curves (**Figure 5**a) at 5 and 10 mg cm^{-2} exhibit a rectangular shape, indicating nearly ideal electrical double-layer capacitive behavior.[13,33] At 20 and 30 mg cm^{-2}, the CV curves slightly distort to a quasi-rectangular shape due to longer electrolyte ion diffusion through the electrode.[7–9] The minor distortion of CV curve shapes at high mass loadings indicates the hierarchical pore structure is retained which still allows effective ion transport to occur in the thicker electrodes used in our studies.

Galvanostatic charge–discharge (GCD) curves at the current density of 1.0 A g^{-1} (Figure 5b) were symmetric and triangular, which further confirms the nearly ideal electrical-double-layer capacitive behavior of 3DG-900 electrodes. In addition, a very small voltage drop (IR drop) is observed at the beginning of the

 © 2024 The Authors. Small Methods published by Wiley-VCH GmbH

23663608, 0, Downloaded from https://onlinelibrary.wiley.com/doi/10.1002/smtd.202301426 by National Energy Technology Laboratory, Wiley Online Library on [11/06/2024]. See the Terms and Conditions (https://onlinelibrary.wiley.com/terms-and-conditions) on Wiley Online Library for rules of use; OA articles are governed by the applicable Creative Commons License

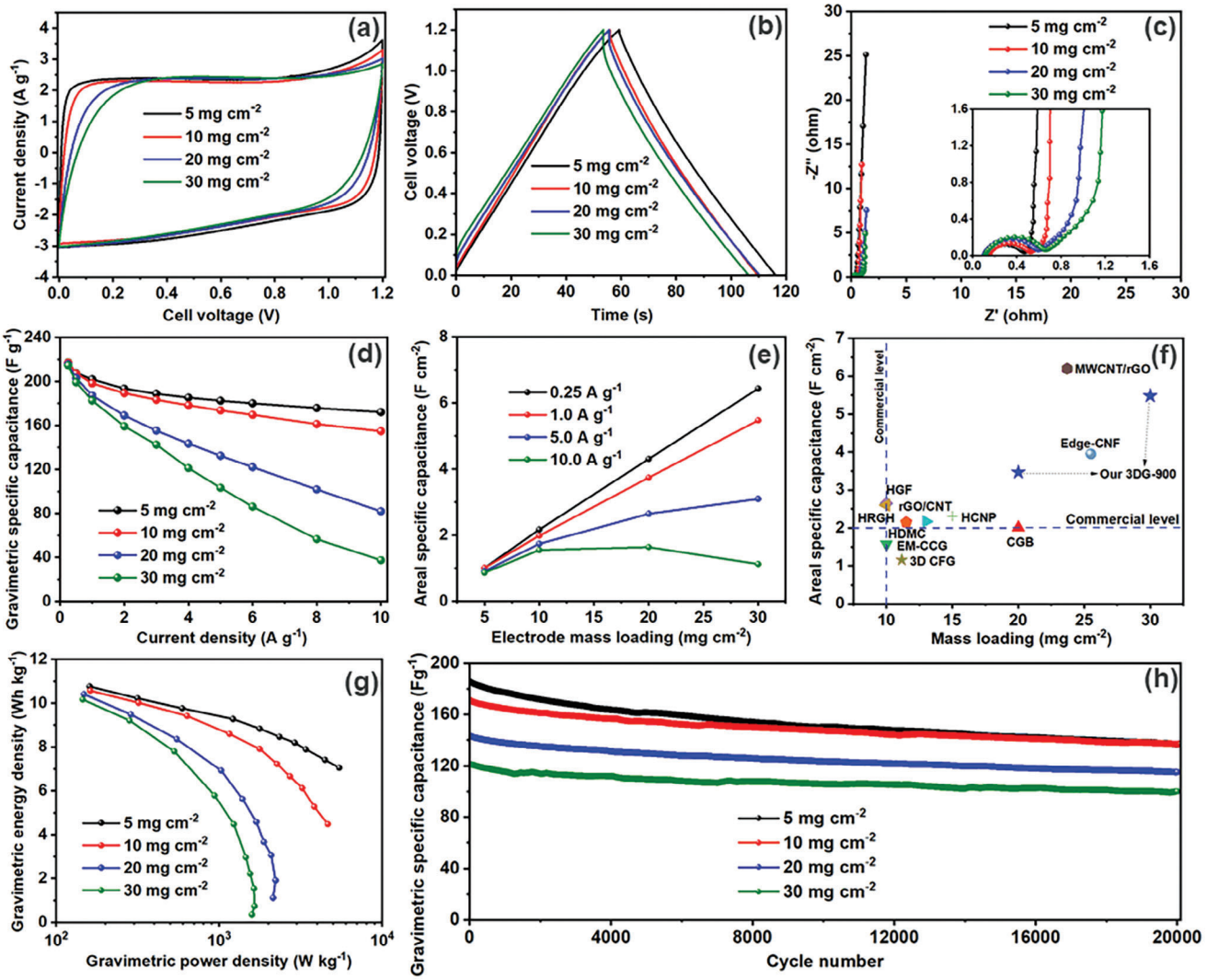

Figure 5. Electrochemical capacitive properties of 3DG-900 supercapacitors with different mass loading using 6 M KOH electrolyte: a) CVs at scan rate of 25 mV s^{-1}, b) GCD curves at current density of 1.0 A g^{-1}, c) Nyquist plots, d) gravimetric rate performance, e) Specific areal capacitances as function of electrode areal mass loading, f) comparison of the specific areal capacitances of 3GD-900 and other high areal mass loading (beyond 10.0 mg cm^{-2}) carbon electrode material at a current density of 1.0 A g^{-1}, tested by two-electrode conFigureuration (Labeling: crumble graphene balls (CGB),[18] 3D cauliflower-fungus-like graphene (3D CFG),[19] holey graphene framework (HGF),[13] hydroxyl-rich graphene hydrogels (HRGH),[12] electrolyte-mediated chemically converted graphene (EM-CCG),[33] partially reduced GO/carbon nanotube composites (rGO/CNT),[34] ten-bilayer hybrid MWCNT/rGO,[35] highly dense mesoporous carbon (HDMC),[16] hollow carbon nanoparticles (HCN),[36] Edge carbon nanofiber (Edge-CNF),[37] g) Ragone plot and h) cycling stability at a current density of 4.0 A g^{-1}.

discharge curve that increased from 0.008 V to 0.021, 0.049, and 0.082 V at electrode areal mass loading of 5.0 to 10.0, 20.0, and 30.0 mg cm^{-2}, respectively, indicating an increase in internal electrode resistance. The equivalent series resistances (ESR) calculated from the IR drops were also very small at 0.60, 0.79, 0.92, and 1.03 ohms, respectively.[42]

Nyquist plots (Figure 5c) show the typical semicircle in the high-frequency region and a nearly vertical line in the low-frequency region, indicating nearly ideal capacitive behavior.[12,13,28,43] The middle-to-high frequency region (Figure 5c, inset) shows 45° lines in the Warburg region which is associated with the resistance from ion diffusion in the electrode.[42,44] The Warburg region gradually increases at higher mass loadings due to a longer ion diffusion distance in these thicker electrodes which suggests that ion diffusion plays a dominant role in controlling the rate capability.[7–9,12] The ESR was determined by extrapolating the vertical portion of the plot to the real axis and was 0.53, 0.68, 0.91, and 1.14 ohms for areal mass loadings of 5.0, 10.0, 20.0, and 30.0 mg cm^{-2}, respectively, which is consistent with the ESR obtained above from IR drops. The small ESR values observed result from the high electrical conductivity and well-preserved hierarchical micro-, meso-, and macro-porous structure of 3DG-900, providing efficient ion transport channels and small ionic resistance.[7–9]

The gravimetric specific capacitances (C_g) of 3GD-900 calculated from the slope of the discharge curves at various current

 © 2024 The Authors. Small Methods published by Wiley-VCH GmbH

23663608, 0, Downloaded from https://onlinelibrary.wiley.com/doi/10.1002/smtd.202301426 by National Energy Technology Laboratory, Wiley Online Library on [11/06/2024]. See the Terms and Conditions (https://onlinelibrary.wiley.com/terms-and-conditions) on Wiley Online Library for rules of use; OA articles are governed by the applicable Creative Commons License

densities are shown in Figure 5d. At a low current density of 0.25 A g^{-1}, C_g was ≈215 F g^{-1} regardless of the areal mass loading. At a medium current density of 1.0 A g^{-1}, C_g decreased slightly from 202, 198, 187, and 182 F g^{-1} at mass loadings of 5, 10, 20, and 30 mg cm^{-2}, respectively. These C_g values are ≈50% higher than what is observed when we evaluate commercial YP-50F activated carbon as a benchmark material under identical testing conditions (Figure S10c, Supporting Information). These C_g values are also comparable to the best values reported for graphene materials in previous literature for high-mass loading supercapacitors (Table S3, Supporting Information). The achievement of high specific capacitance at ultrahigh mass loading resulted in ultrahigh areal capacitance of 3DG-900. Figure 5e displays the linear increase of areal capacitance with an increase of mass loading, up to 6.44 F cm^{-2} at the current density of 0.25 A g^{-1}, which is more than 3 times higher than current commercial requirement.[7–9] Even at a medium current density of 1.0 A g^{-1}, the areal capacitance of 3DG-900 was still as high as 5.48 F cm^{-2}, which is the second-best value reported for carbonaceous materials at high mass loadings (Figure 5f; Table S3, Supporting Information).

The combination of ultrahigh areal capacitance with an extended working voltage of 1.2 V resulted in ultrahigh areal energy density, up to 0.30 mWh cm^{-2} at a power density of 4.4 mW cm^{-2} (Figure S11d, Supporting Information). This is significantly higher than previous reports for comparable carbons such as: heteroatom-doped pillared porous carbon (AMJ-3, 0.21 mWh cm^{-2} at 1.0 mW cm^{-2}),[45] edge-enriched carbon nanofiber fabric (Edge-CNF, 0.1375 mWh cm^{-2} at 6.4 mW cm^{-2}),[37] and graphene/carbon nanofiber films (NG/CNFs, 0.22 mWh cm^{-2} at 1.0 mW cm^{-2}).[46]

3DG-900 also has an outstanding gravimetric energy density of ≈10 Wh kg^{-1} regardless of areal mass loading (Figure 5g), which is higher than previous reports for high mass loading carbon electrode supercapacitors using aqueous electrolytes (Table S3, Supporting Information). At commercial level mass loadings of 10 mg cm^{-2}, 3DG-900 also displayed an excellent energy density of 4.5 Wh kg^{-1} at a power density of 4650 W kg^{-1}, suggesting it is well-suited for high-power supercapacitor application. Figure 5h shows the excellent cycling stability of 3DG-900 with capacitance retention of ~80% after 20000 cycles at a current density of 4.0 A g^{-1}, highlighting the stability of this material and its potential for use in practical supercapacitor devices. More interestingly, 3DG-900 with higher areal mass loadings exhibited slightly better cycling stability which might be explained by slightly better coulombic efficiency, which is >99.8% of 3DG-900 with mass loadings of 20 and 30 mg cm^{-2} (Figure S11e, Supporting Information).

2.3. Synthesis of 3D Graphenes with Recycled Potassium Carbonate

Synthesizing 3DG-900 on a large scale could present challenges due to the material, processing, and waste costs associated with using large amounts of K_2CO_3 as a catalyst and activating agent. It is however feasible to recycle and recover the K_2CO_3 from the rinse water in our process to improve the cost-effectiveness and sustainability of the synthesis process described in this work.

Specifically, a small quantity of K_2CO_3 is consumed during the activation redox reaction with CTP at above 600 °C and converted to K and CO (gas):

$$K_2CO_3 + 2C \rightarrow 2K + 3CO \quad (1)$$

Partial decomposition of K_2CO_3 also occurs above 800 °C during the graphenization process to form K_2O and CO_2 (gas):[47]

$$K_2CO_3 \rightarrow K_2O + CO_2 \quad (2)$$

The K and K_2O byproducts from these steps are both converted into KOH during the water rinsing step:

$$2K + 2H_2O \rightarrow 2KOH + H_2 \quad (3)$$

$$K_2O + H_2O \rightarrow 2KOH \quad (4)$$

It is therefore possible to recycle the K_2CO_3 and KOH salt mixture in the rinse water by neutralizing the KOH byproduct with $KHCO_3$ and drying the rinse water to recover K_2CO_3 as a solid salt that can be reused in subsequent graphenization cycles:

$$KOH + KHCO_3 \rightarrow K_2CO_3 + H_2O \quad (5)$$

The detailed steps involved in the recycling and recovery process are described in the experimental section. **Figure 6** shows representative SEM, Raman, and N_2 isotherms of 3D graphenes synthesized with recycled K_2CO_3 at the graphenization temperature of 900 °C, denoted as 3DG-900-RE*x*, where *x* is the number of times the K_2CO_3 has been recycled. Figure 6a–d for 3DG-900-RE*x* shows the same hierarchical, interconnected, 3D networks of thin, crumpled, graphene sheets and overall macro- and meso-scale pore structures as observed in Figure 2 for samples made with fresh K_2CO_3. The Raman spectra of 3DG-900-RE*x* also exhibited prominent D, G, and 2D bands with I_D/I_G in the range of 0.50–0.57 (Table S4, Supporting Information), slightly lower than that of 3DG-900. The N_2 isotherms of 3DG-900-RE*x* showed similarly patterned curves with BET SSA of 2000–2080 m^2 g^{-1} and total pore volumes of 1.47–1.83 cm^3 g^{-1} (Table S4, Supporting Information), which is only slightly lower than that of 3DG-900. Moreover, the C/O ratio of 3DG-900-RE*x* determined by XPS ranged from 47.8 to 57.8, slightly higher than 3DG-900. It is interesting to note that the slightly lower textural properties of 3DG-900-RE*x* may be a result of a higher degree of graphenization as evidenced by the slightly lower Raman I_D/I_G and higher C/O ratio.

The electrochemical capacitive properties of 3DG-900-RE*x* supercapacitors with commercial-level areal mass loading were shown together with 3DG-900 in **Figure 7**. The CVs of 3DG-900-RE*x* displayed a nearly rectangular shape, almost identical to 3DG-900 but somewhat smaller response current densities, implying slightly smaller specific capacitances. The GCD curves of 3DG-900-RE*x* were also symmetrically triangular with very small IR drops, similar to 3DG-900 but with a slightly slower response time. The Nyquist plots (Figure 7c) of 3DG-900-RE*x* were identical to 3DG-900 with a very small semicircle in the high-frequency region and a nearly vertical line in the low-frequency region, indicating the nearly ideal capacitive behavior. The close-up inset

© 2024 The Authors. Small Methods published by Wiley-VCH GmbH

23669608, 0, Downloaded from https://onlinelibrary.wiley.com/doi/10.1002/smtd.202301426 by National Energy Technology Laboratory, Wiley Online Library on [11/06/2024]. See the Terms and Conditions (https://onlinelibrary.wiley.com/terms-and-conditions) on Wiley Online Library for rules of use; OA articles are governed by the applicable Creative Commons License

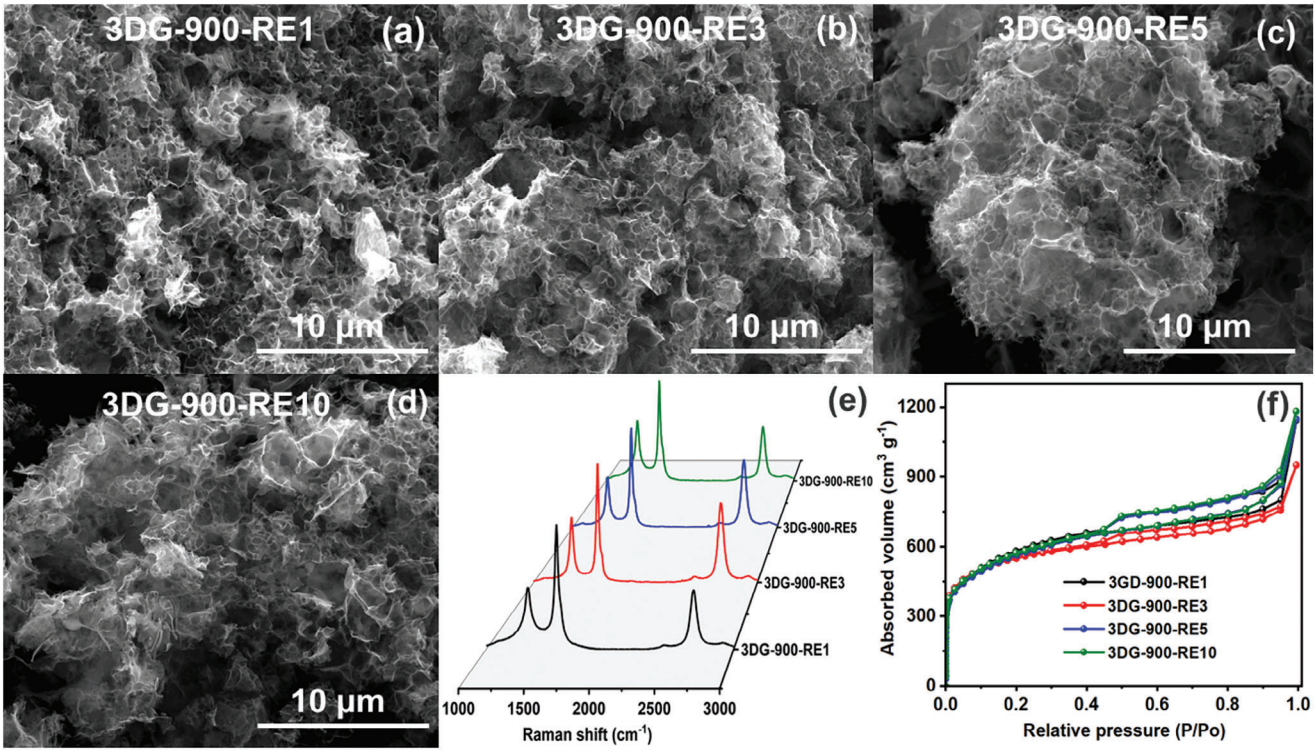

Figure 6. a–d) SEM images, e) Raman spectra, and f) N2 isotherms of 3DG-900-RE1, 3DG-900-RE3, 3DG-900-RE5, and 3DG-900-RE10.

shows the ESR of 3DG-900-RE*x* and 3DG-900 were very similar, in the range of only 0.65 to 0.75 ohm. Figure 7d shows the specific capacitance of 3DG-900-RE*x* to be ≈195–200 F g^{-1} at a current density of 0.25 A g^{-1}, in comparison to 215 F g^{-1} measured for 3DG-900. The slightly smaller specific capacitance of 3DG-900-RE*x* could be attributed to their slightly lower BET SSA. The cycling stability of 3DG-900-RE*x* was similar to that of 3DG-900, ≈85–90% capacitance retention after 10 000 cycles.

Overall, 3DG-900-RE*x* shows consistency in physical and electrochemical capacitive properties over 10 cycles, suggesting it is possible to recycle the K_2CO_3 further. To the best of our knowledge, this is the first and only report on recycling the K_2CO_3 activation agent which is commonly used for converting carbon feedstocks into graphene and porous carbons.

2.4. Discussion

The 3DG samples were synthesized using K_2CO_3 and CTP which are a common activating agent and carbon feedstock, respectively, for the synthesis of amorphous porous carbons.[48–51] The graphenization activity of K_2CO_3 was not recognized until Xia et al. reported the formation of 3D porous graphene-like sheets (3DPGLS) by thermal treatment of coconut shell char with K_2CO_3 at 900 °C.[21] We find that the synthesis method and use of solid carbon feedstocks reported by Xia et. al. only result in the graphenization on the surface of the carbon particle. Our results with solid bituminous coal char (BCC) and a solid porous spent coffee ground char (SCGC) feedstocks (Figure S12, Supporting Information) show that only the surface region of the carbon particle is graphenized leaving an amorphous carbon core in the sample. Our result is consistent with the Raman mapping from Xia et. al. on samples flattened by glass slides that show regions in their sample with high graphenization, as well as regions of amorphous carbon with low- or no- graphenization. We believe the surface-restricted graphenization reaction of K_2CO_3 is a fundamental characteristic of using larger particles of solid carbon feedstock with the precise synthesis method reported by Xia et. al. due to the limited contact between solid carbon feedstock with the K_2CO_3 catalyst.

In this paper, we address this challenge by using a CTP feedstock with a high ratio of K_2CO_3 to carbon (Figure 1). CTP, unlike solid carbon, melts upon heating and coats the surface of K_2CO_3 particles, as well as the spaces between these particles. The high K_2CO_3 to carbon ratio ensures that the melted CTP is then carbonized into a 3D network of very thin carbon nanosheets which allow direct, intimate contact between the catalyst and carbon precursor. The carbon nanosheets are subsequently graphenized above the melting point of K_2CO_3 into graphene sheets. Our process also works with petroleum pitch (Figure S13, Supporting Information). The use of carbon pitch feedstocks as well as the high K_2CO_3 to carbon ratio are unique facets of our synthesis method that have not been explored in previous literature and that result in the quality and electrocapacitive performance of 3DG samples reported in this paper.

The synthesis method reported here uses inexpensive, commercially available, reagents (K_2CO_3 and pitch) along with simple thermal processing under an inert atmosphere to produce a high surface area, conductive carbon that possesses remarkable

 © 2024 The Authors. Small Methods published by Wiley-VCH GmbH

23669608, 0, Downloaded from https://onlinelibrary.wiley.com/doi/10.1002/smtd.202301426 by National Energy Technology Laboratory, Wiley Online Library on [11/06/2024]. See the Terms and Conditions (https://onlinelibrary.wiley.com/terms-and-conditions) on Wiley Online Library for rules of use; OA articles are governed by the applicable Creative Commons License

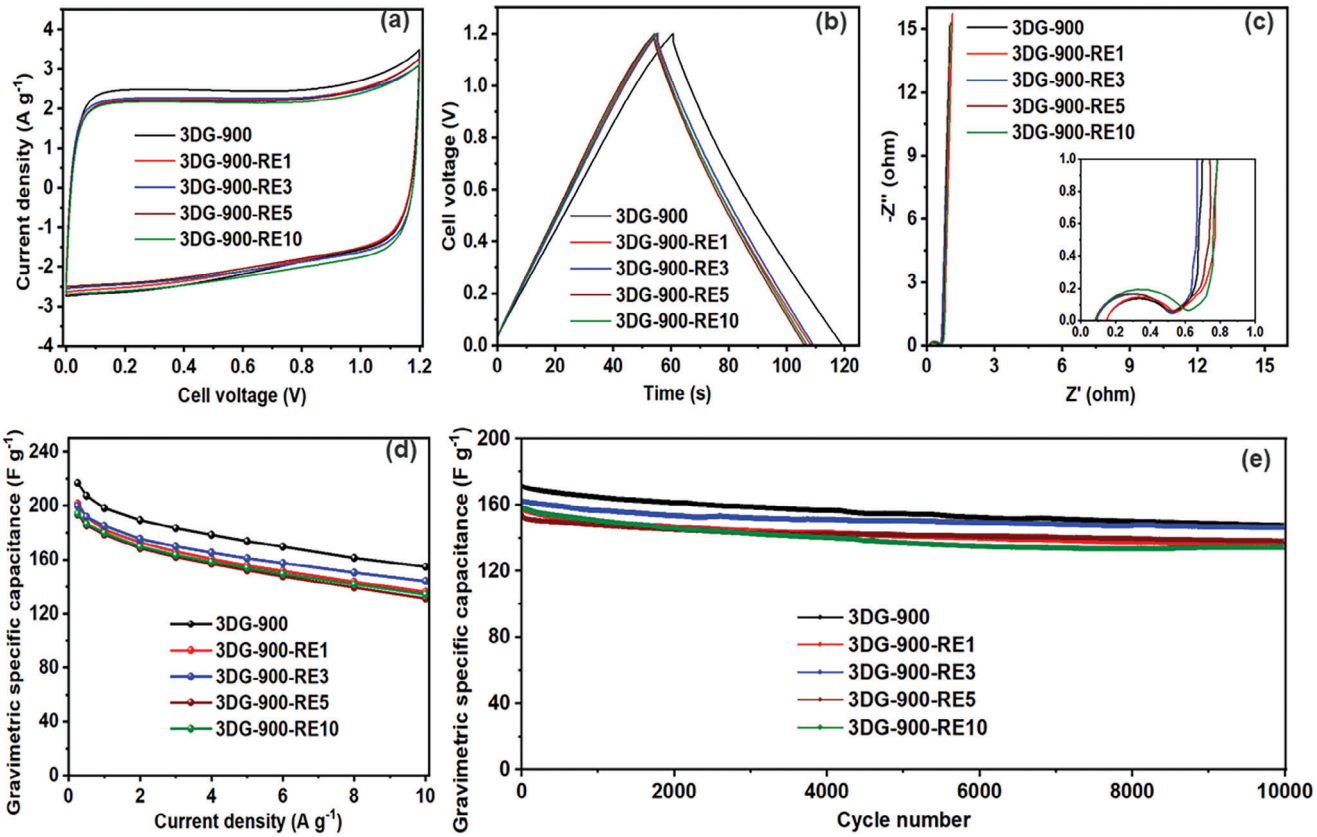

Figure 7. Electrochemical capacitive properties of 3DG-900-RE*x* and 3DG-900 supercapacitors with mass loading of 10 mg cm^{-2}: a) CVs at a scan rate of 25 mV s^{-1}, b) GCD curves at a current density of 1.0 A g^{-1}, c) Nyquist plots, d) gravimetric rate performance, e) cycling stability at a current density of 4.0 A g^{-1}.

supercapacitor performance properties at a commercial-level mass loading and thickness. The carbon material produced in this work performs significantly better across nearly all electrocapacitive performance metrics than previously reported literature (Table S3, Supporting Information). The simple synthesis method and unique electrocapacitive properties at commercial-level mass loadings and thickness make our results highly relevant for the production and engineering of practical supercapacitor devices. Moreover, the high specific surface area (~2100 m^2 g^{-1}), high pore volume (~1.8 cm^3 g^{-1}), superior electrical conductivity, and 3D interconnected hierarchical micro/meso/macroporous structures make 3DG-900 a promising electrode material for other electrochemical applications such as cathode hosts for lithium-sulfur batteries and zinc-iodine batteries, cathode materials for hybrid capacitors and electrochemical catalyst supports.

3. Conclusion

In summary, we reported a facile method to synthesize high-quality microscopic 3D graphenes with BET SSA up to 2100 m^2 g^{-1}, the highest value reported for 3D graphene, which exhibited outstanding electrochemical capacitive properties with ultrahigh areal capacitance more than 6 F cm^{-2}, excellent energy density of >10 Wh kg^{-1} and superior cycling stability of ~80% capacitance retention after 20 000 cycles with extended working voltage of 1.2 V with 6 M KOH electrolyte. More importantly, for the first time in literature, we demonstrated the process of recycling template and catalyst agent for graphene synthesis for at least 10 cycles, resulting in low-cost and sustainable production. The achievement of facile, low-cost, and sustainable production of such high-quality graphene with outstanding capacitive properties at ultra-high mass loading would open up exciting opportunities for the application of graphene in supercapacitors at commercial scale.

4. Experimental Section

Synthesis of 3D Graphenes: Three-dimensional graphene was synthesized by ball-milling of 2.0 g coal tar pitch with 20.0 g K_2CO_3 (mass ratio of 1:10) for 15 min, followed by heating to 600 °C at a ramping rate of 10 °C min^{-1} for 2.0 h for carbonization and then continue heating to 900 and 950 °C for 2.0 h or 1000 °C for 1 h for catalytic graphenization under a nitrogen atmosphere. After natural cooling, the obtained sample was washed twice with DI water by adding the sample into 150 mL water, mixed, and heated to 80 °C for 1 h, subsequently suction filtrated. The attained filtered cake was washed with 1.0 M hydrochloric acid solution (80 °C, 2 h) and then with DI water until neutral pH and finally dried at 150 °C for 5 h. The obtained 3D graphene samples were denoted as 3DG-x where x is graphenization temperature.

The recycling of K_2CO_3 was carried out by collecting filtrates in the first two washes with DI water, neutralizing with 1.0 g potassium bicarbonate ($KHCO_3$), and drying at 200 °C for 6 h. The obtained recycled K_2CO_3

 © 2024 The Authors. Small Methods published by Wiley-VCH GmbH

23669608, 0, Downloaded from https://onlinelibrary.wiley.com/doi/10.1002/smtd.202301426 by National Energy Technology Laboratory, Wiley Online Library on [11/06/2024]. See the Terms and Conditions (https://onlinelibrary.wiley.com/terms-and-conditions) on Wiley Online Library for rules of use; OA articles are governed by the applicable Creative Commons License

(~20.0 g) was ground and then ball-milled with 2.0 g coal tar pitch, followed by pre-carbonization, catalytic graphenization, and washing with the same procedures as described above. The obtained 3D graphene samples were denoted as 3DG-*x*-RE*y* where *x* and *y* are graphenization temperature and recycle time, respectively.

Materials Characterization: Scanning electron microscopy (SEM) imaging was carried out on an FEI Quanta 600F microscope operated at 10–20 kV equipped with an energy-dispersive X-ray (EDX) detector. High-resolution transmission electron microscopy (HR-TEM) was performed on a FEI Titan Themis G2 200 Probe Cs Corrected Scanning Transmission Electron Microscope operated at an accelerating voltage of 200 kV. Raman spectroscopy was conducted on a LabRam HR-Evolution spectrometer (Horiba Scientific) with a 532 nm laser as an excitation source. X-ray photoelectron spectroscopy (XPS) was carried out on a PHI 5000 VersaProbe III scanning XPS microprobe (Physical Electronics, ULVAC-PHI Inc) using Al Kα (1486.6 eV) radiation source and a hemispherical analyzer. X-ray powder diffraction (XRD) patterns were characterized on a PANalytical X'Pert Pro X-ray diffractometer using CuKα radiation (λ = 1.5418 Å) at a scan rate of 1.0 degree min^{-1}. N_2 adsorption–desorption isotherms analysis was measured on Quantachrome Autosorb-1 at −196 °C. For electrical conductivity measurement, 3DG samples were mixed with polytrafluoroethylene (PTFE, 5 wt%) in methanol, sonicated for 5 min, dried at 120 °C for 3 h and then compressed into 200 µm pellet using an FTIR sampling kit under a compression force of 4.0 tons cm^{-2} for 30 s. The sheet resistance of 3DG pellets was measured on a four-point probe Jandel RM3-AR and electrical conductivity (σ (S m^{-1})) of 3DG pellets was calculated by $\sigma = 1/R_s t$ where R_s is sheet resistance (Ω) and t is pellet thickness (m).

Electrode Fabrication and Electrochemical Performance Characterization: 3DG-900 electrodes were fabricated by mixing 95.0 mg and 5.0 mg PTFE binder in 10 mL methanol alcohol, sonicating for 5 min, and then dried at 120 °C for 3 h. The obtained powders were compressed into free-standing electrode pellets (1.3 cm in diameter, corresponding to 1.33 cm^2 in area) with different mass loadings (5.0, 10.0, 20.0, and 30.0 mg cm^{-2}) using an FTIR sampling kit with 13 mm pellet die by hydraulic press under compression force of 4.0 tons cm^{-2} for 30 s. It is necessary to compress this material to make a compact and robust electrode, especially at high mass loadings. This compression improves the electrochemical capacitive performance of the 3D graphene reported in this paper. Symmetric supercapacitors with a two-electrode configuration were fabricated using two identical electrodes as both anode and cathode sandwiched between two nickel foam current collectors, a cellulose filter paper (Whatman) as a separator sandwiched between two electrodes, and an aqueous solution of 6 M KOH as electrolytes. All the components were assembled into a layered structure and were tightly sealed in a supercapacitor test cell (EQ-STC split flat cell, MTI Corp.). Cyclic voltammetry and galvanostatic charge–discharge measurements were performed on a potentiostat/galvanostat Biologic SP-150. Electrochemical impedance spectroscopy tests were recorded over a frequency range from 0.01 Hz to 200 kHz at an open-circuit potential with an AC perturbation of 10.0 mV. The gravimetric and areal-specific capacitance, energy density, and power density were calculated according to the following equations:

$$C_g = 4\left(\frac{I\Delta t}{m\Delta V}\right) \quad (6)$$

$$C_a = \frac{mC_g}{A} \quad (7)$$

$$E_g = \frac{1}{8}C_g(\Delta V)^2 \quad (8)$$

$$P_g = \frac{E_g}{\Delta t} \quad (9)$$

where C_g and C_a are the gravimetric and areal-specific capacitances, E_g and P_g are the gravimetric energy density and power density, respectively. I is the constant discharge current, Δt is the discharging time, m and A are the mass and area of two electrodes, and ΔV is the operating voltage (obtained from the discharge curve subtracted by the voltage drop).

Supporting Information

Supporting Information is available from the Wiley Online Library or from the author.

Acknowledgements

This work was performed in support of the US Department of Energy's Fossil Energy and Carbon Management's (FECM) Carbon Ore Processing Program.

Conflict of Interest

The authors declare no conflict of interest.

Data Availability Statement

The data that support the findings of this study are available in the supplementary material of this article.

Keywords

3D graphene, catalytic graphenization, supercapacitor

Received: October 17, 2023
Revised: April 17, 2024
Published online:

[1] Z. Zhu, T. Jiang, M. Ali, Y. Meng, Y. Jin, Y. Cui, W. Chen, *Chem. Rev.* **2022**, *122*, 16610.
[2] T. M. Gür, *Energy Environ. Sci.* **2018**, *11*, 2696.
[3] F. Díaz-González, C. Chillón-Antón, M. Llonch-Masachs, S. Galceran-Arellano, J. Rull-Duran, J. Bergas-Jané, E. Bullich-Massagué, *J. Energy Storage* **2022**, *51*, 104446.
[4] P. C. Denholm, C. Wesley, A. W. Frazier, K. Podkaminer, N. Blair, National Renewable Energy Laboratory, US Department of Energy (DOE) energy report, **2021**, https://doi.org/10.2172/1763974.
[5] J. Liu, J. Wang, C. Xu, H. Jiang, C. Li, L. Zhang, J. Lin, Z. X. Shen, *Adv. Sci.* **2018**, *5*, 1700322.
[6] H. Shao, Y.-C. Wu, Z. Lin, P.-L. Taberna, P. Simon, *Chem. Soc. Rev.* **2020**, *49*, 3005.
[7] L. Chang, Y. H. Hu, *Matter* **2019**, *1*, 596.
[8] Y. Dong, J. Zhu, Q. Li, S. Zhang, H. Song, D. Jia, *J. Mater. Chem. A* **2020**, *8*, 21930.
[9] W. Guo, C. Yu, S. Li, J. Qiu, *Energy Environ. Sci.* **2021**, *14*, 576.
[10] Z. Sun, S. Fang, Y. H. Hu, *Chem. Rev.* **2020**, *120*, 10336.
[11] J. Han, I. Johnson, M. Chen, *Adv. Mater.* **2022**, *34*, 2108750.
[12] H. Ma, Q. Zhou, M. Wu, M. Zhang, B. Yao, T. Gao, H. Wang, C. Li, D. Sui, Y. Chen, G. Shi, *J. Mater. Chem. A* **2018**, *6*, 6587.
[13] Y. Xu, Z. Lin, X. Zhong, X. Huang, N. O. Weiss, Y. Huang, X. Duan, *Nat. Commun.* **2014**, *5*, 4554.
[14] Z. Chen, W. Ren, L. Gao, B. Liu, S. Pei, H.-M. Cheng, *Nat. Mater.* **2011**, *10*, 424.
[15] L. Chang, D. J. Stacchiola, Y. H. Hu, *J. Mater. Chem. A* **2017**, *5*, 23252.
[16] L. Chang, K. Sun, Y. H. Hu, *ACS Appl. Mater. Interfaces* **2018**, *10*, 33162.
[17] X. Wang, Y. Zhang, C. Zhi, X. Wang, D. Tang, Y. Xu, Q. Weng, X. Jiang, M. Mitome, D. Golberg, Y. Bando, *Nat. Commun.* **2013**, *4*, 2905.

 © 2024 The Authors. Small Methods published by Wiley-VCH GmbH

23669608, 0, Downloaded from https://onlinelibrary.wiley.com/doi/10.1002/smtd.202301426 by National Energy Technology Laboratory, Wiley Online Library on [11/06/2024]. See the Terms and Conditions (https://onlinelibrary.wiley.com/terms-and-conditions) on Wiley Online Library for rules of use; OA articles are governed by the applicable Creative Commons License

[18] J. Luo, H. D. Jang, J. Huang, *ACS Nano* **2013**, *7*, 1464.
[19] L. Chang, W. Wei, K. Sun, Y. H. Hu, *J. Mater. Chem. A* **2015**, *3*, 10183.
[20] Y. Gogotsi, P. Simon, *Science* **2011**, *334*, 917.
[21] J. Xia, N. Zhang, S. Chong, D. Li, Y. Chen, C. Sun, *Green Chem.* **2018**, *20*, 694.
[22] S. W. Kim, K. Uematsu, K. Toda, M. Sato, *J. Ceram. Soc. Jpn.* **2015**, *123*, 355.
[23] Y. Li, J. Chen, L. Huang, C. Li, J.-D. Hong, G. Shi, *Adv. Mater.* **2014**, *26*, 4789.
[24] C. Zhu, T. Y.-J. Han, E. B. Duoss, A. M. Golobic, J. D. Kuntz, C. M. Spadaccini, M. A. Worsley, *Nat. Commun.* **2015**, *6*, 6962.
[25] Z. Xu, Y. Zhang, P. Li, C. Gao, *ACS Nano* **2012**, *6*, 7103.
[26] Y. Yoon, K. Lee, C. Baik, H. Yoo, M. Min, Y. Park, S. M. Lee, H. Lee, *Adv. Mater.* **2013**, *25*, 4437.
[27] M.-Q. Zhao, Q. Zhang, J.-Q. Huang, G.-L. Tian, J.-Q. Nie, H.-J. Peng, F. Wei, *Nat. Commun.* **2014**, *5*, 3410.
[28] Y. Li, Z. Li, P. K. Shen, *Adv. Mater.* **2013**, *25*, 2474.
[29] X.-F. Jiang, R. Li, M. Hu, Z. Hu, D. Golberg, Y. Bando, X.-B. Wang, *Adv. Mater.* **2019**, *31*, 1901186.
[30] J. Cao, C. Zhu, Y. Aoki, H. Habazaki, *ACS Sustainable Chem. Eng.* **2018**, *6*, 7292.
[31] J. Jeong, M. Choun, J. Lee, *Angew. Chem., Int. Ed.* **2017**, *56*, 13513.
[32] M. S. Kang, I. Heo, K. G. Cho, H. Kyung, H. S. Kim, K. H. Lee, W. C. Yoo, *Energy Storage Mater.* **2022**, *45*, 380.
[33] X. Yang, C. Cheng, Y. Wang, L. Qiu, D. Li, *Science* **2013**, *341*, 534.
[34] N. Díez, C. Botas, R. Mysyk, E. Goikolea, T. Rojo, D. Carriazo, *J. Mater. Chem. A* **2018**, *6*, 3667.
[35] Y. Yang, Q. Huang, L. Niu, D. Wang, C. Yan, Y. She, Z. Zheng, *Adv. Mater.* **2017**, *29*, 1606679.
[36] C. Fan, Y. Dong, Y. Liu, L. Zhang, D. Wang, X. Lin, Y. Lv, S. Zhang, H. Song, D. Jia, *Carbon* **2020**, *160*, 328.
[37] J. Zhu, L. Wang, X. Gan, T. Tang, F. Qin, W. Luo, Q. Li, N. Guo, S. Zhang, D. Jia, H. Song, *Energy Storage Mater.* **2022**, *47*, 158.
[38] Y.-W. Chi, C.-C. Hu, H.-H. Shen, K.-P. Huang, *Nano Lett.* **2016**, *16*, 5719.
[39] C.-F. Liu, Y.-C. Liu, T.-Y. Yi, C.-C. Hu, *Carbon* **2019**, *145*, 529.
[40] Z. Yang, J. Tian, Z. Yin, C. Cui, W. Qian, F. Wei, *Carbon* **2019**, *141*, 467.
[41] M. Yu, Y. Lu, H. Zheng, X. Lu, *Chemistry* **2018**, *24*, 3639.
[42] S. Zhang, N. Pan, *Adv. Energy Mater.* **2015**, *5*, 1401401.
[43] W. Tian, J. Zhu, Y. Dong, J. Zhao, J. Li, N. Guo, H. Lin, S. Zhang, D. Jia, *Carbon* **2020**, *161*, 89.
[44] B.-A. Mei, O. Munteshari, J. Lau, B. Dunn, L. Pilon, *J. Phys. Chem. C* **2018**, *122*, 194.
[45] Y. Zhao, C. Dong, L. Sheng, Z. Xiao, L. Jiang, X. Li, M. Jiang, J. Shi, *ACS Sustainable Chem. Eng.* **2020**, *8*, 8664.
[46] R. Zhang, J. Yan, L. Wang, W. Shen, J. Zhang, M. Zhong, S. Guo, *J. Power Sources* **2021**, *513*, 230559.
[47] M.-J. Kim, S. W. Choi, H. Kim, S. Mun, K. B. Lee, *Chem. Eng. J.* **2020**, *397*, 125404.
[48] P. R. Choi, J. C. Jung, Y.-S. Lim, M.-S. Kim, *Han'guk Chaelyo Hakhoechi* **2016**, *26*, 460.
[49] N. Díez, G. A. Ferrero, A. B. Fuertes, M. Sevilla, *Batteries Supercaps* **2019**, *2*, 701.
[50] M. Sevilla, N. Díez, A. B. Fuertes, *ChemSusChem* **2021**, *14*, 94.
[51] M. Sevilla, A. B. Fuertes, *ChemSusChem* **2016**, *9*, 1880.

 © 2024 The Authors. Small Methods published by Wiley-VCH GmbH

23663608, 0, Downloaded from https://onlinelibrary.wiley.com/doi/10.1002/smtd.202301426 by National Energy Technology Laboratory, Wiley Online Library on [11/06/2024]. See the Terms and Conditions (https://onlinelibrary.wiley.com/terms-and-conditions) on Wiley Online Library for rules of use; OA articles are governed by the applicable Creative Commons License